"Synchrotron Radiation and Applications, the X-Ray Standing Wave Technique: Principles and Applications" (World Scientific) Ed. J. Zegenhagen and A. Kazimirov, (2012).

Chapter 7

X-RAY STANDING WAVE IN MULTILAYERS

Michael J. Bedzyk

Department of Materials Science and Engineering,
Northwestern University Cook Hall, Evanston, IL 60208,
USA and Argonne National Laboratory
Argonne, IL 60439, USA

Joseph A. Libera

Energy Systems Division, Argonne National Laboratory,
9700 S. Cass Ave
Argonne, IL 60439, USA

An extension of Fresnel theory is used to describe how reflectivity from a periodic multilayer mirror generates an X-ray Standing Wave (XSW) above the mirror surface. This long-period XSW is used to study distribution profiles of atoms within deposited ultrathin organic films and ions at the liquid–solid interface.

7.1. Introduction

In Chapter 5, the case of generating a long-period X-ray standing wave (XSW) by total reflection from a mirror surface was discussed. The TR-XSW method is used to determine the X-ray fluorescence (XRF)-selected atomic density profile $\rho(z)$ in a surface over-layer structure by measuring its Fourier transform in the low-Q range that extends up to $Q_{\max} \sim 1.6 \bullet Q_C$. Beyond this nominal limit, which is about 0.1 Å^{-1} for a gold mirror, the reflectivity from a simple mirror and the associated XSW fringe visibility become too weak for producing measurable XRF modulations.

In this chapter, we discuss how to extend the Q-range and thereby improve the $\pi/Q_{\max}$ intrinsic resolution of the long-period XSW method

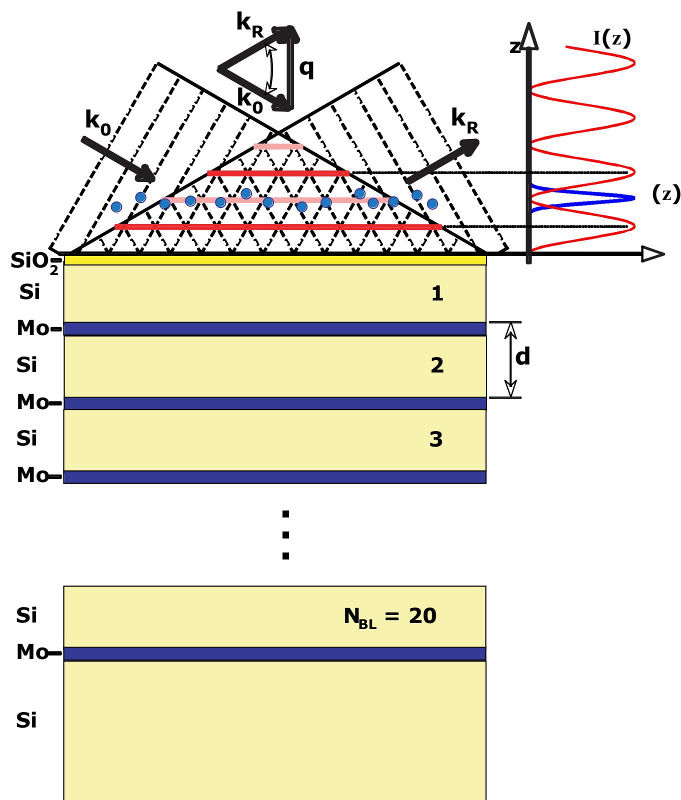

Fig. 7.1. Illustration of XSW generated by first-order Bragg diffraction from a Si/Mo periodic multilayer (PML). For $\lambda = 1\mathring{A}$ and $d = 200\mathring{A}$, the incident angle is much smaller than depicted. Refraction effects at this very small incident angle cause the XSW period above the PML surface, $D = \lambda/(2sin\theta)$, to be smaller than d.

by replacing the simple mirror with a periodic multilayer (PML) as depicted in Fig. 7.1. The XSW effect can then be observed over the $m = 0$, $m = 1$, and higher-order Bragg peaks and used for determining $\rho(z)$ for an atomic distribution contained within an overlayer that resides above the PML surface. Case studies include overlayers of sputter-deposited metal atoms,[1] electrochemically deposited metal atoms,[2] Langmuir–Blodgett multilayers,[3] organo–metallic multilayers,[4] and biomolecular adsorption at charged liquid–solid interfaces.[5] The XSW internal to the PML can also be used for characterizing the internal micro- or nanostructure of the PML,[6–10] or even the magnetic structure when coupled with circular-magnetic dichroism.[11]

For Bragg diffraction purposes, a layered synthetic microstructure (LSM) is fabricated (typically by sputter deposition) to have a depth-periodic layered structure consisting of 10 to 200 layer pairs of alternating high- and low-electron density materials such as Mo and Si. Such periodic multilayers are primarily used as soft X-ray monochromators and analyzers[12–14] and as hard X-ray wide-band pass monochromators.[15,16] Sufficient lateral uniformity in layer thickness is attainable in the range between 10 and 150 Å (*d*-spacing of fundamental diffraction planes from 20 Å to 300 Å). Because of the rather low number of layer pairs that affect Bragg diffractions, these optical elements have a significantly wider energy band-pass and angular reflection width than do single crystals. For XSW measurements, the required quality of a PML is that its experimental reflection curve compares well with dynamical diffraction theory, and that the $m = 1$ Bragg peak reflectivity is typically higher than 70%. With this, a well-defined XSW can be generated and used to probe structures deposited on a PML surface with a periodic scale equivalent to the rather large *d*-spacing. To a good approximation, the first-order Bragg diffraction planes coincide with the centers of the high-density layers of the PML. Above the surface of the PML, the XSW period is $\mathrm{D} = \lambda/(2\sin\theta)$; just as it was defined in ~~the~~ Chapter 5 for TR-XSW. As discussed later in this chapter, the reflectivity $R(Q)$ can be calculated from Parratt's recursion formulation.[17] This same optical theory is then extended to allow the calculation of the E-field intensity, $I(Q, z)$, at any position z within any of the slabs. This is then used to calculate the yield from an XRF-selected atomic species.

7.2. Calculating the X-Ray Fields within a Multilayer Structure

In Fig. 7.2, the multilayer will be described as a stratified medium with M homogeneous layers. Each layer has a thickness t_j and an index of refraction $n_j = 1 - \delta_j - i\beta_j$. The semi-infinitely thick $j = 1$ top layer will be vacuum (or air) with $n = 1$, and the $j = M$ bottom layer will be the semi-infinitely thick substrate. The layers just below the vacuum layer can simulate the overlayer structure, and just below that can be placed the periodic multilayer (or a simple mirror). Since each layer is treated individually, it is possible to simulate a graded d-spacing rather than having an ideally periodic multilayer. It is also possible to introduce extra sets of layers for simulating graded interface structures[18] that account for interface diffusion with individually tailored profiles.

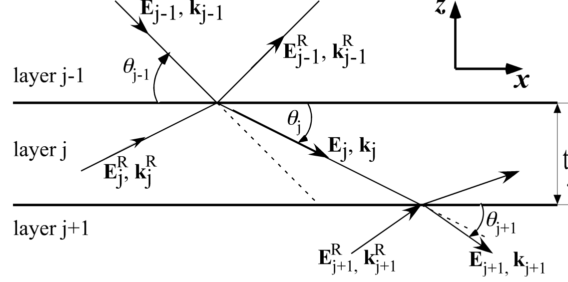

Fig. 7.2. The reflection and refraction of E-M plane-waves at two successive boundaries in a multilayer. The boundaries are parallel and separate layers $j-1, j$ and $j+1$ with indices of refraction $n_{j-1} > n_{j+1} > n_j$.

An electromagnetic plane wave impinging on such a stratified multilayer medium is a classic problem described in several textbooks.[19] We will follow the treatment of Parratt,[17] who studied the case at X-ray frequencies. Parratt's derivation, which was aimed at calculating the reflectivity in vacuum, will be modified for the XSW case to make it possible to calculate the E-field intensity at any point within the multilayer.[20]

For the σ-polarization case, the continuity of tangential components of the E-field and the H-field vectors at the $j, j+1$ boundary leads to the following pair of equations for the E-fields at depth z_j and z_{j+1} below the top interface of layer j and $j+1$, respectively.

$$\begin{aligned} a_j E_j(z_j) + a_j^{-1} E_j^R(z_j) &= b_{j+1}^{-1} E_{j+1}(z_{j+1}) + b_{j+1} E_{j+1}^R(z_{j+1}) \\ (a_j E_j(z_j) - a_j^{-1} E_j^R(z_j)) n_j \theta_j &= (b_{j+1}^{-1} E_{j+1}(z_{j+1}) \\ &\quad - b_{j+1} E_{j+1}^R(z_{j+1})) n_{j+1} \theta_{j+1} \end{aligned} \tag{7.1}$$

where the E-fields within the jth layer at a depth z_j below the $j-1, j$ interface are expressed as:

$$E_j(z_j) = E_j(0)\exp(-ik_j \sin\theta_j z_j) = E_j(0)\exp\left(-i\frac{1}{2}Q_j z_j\right) \tag{7.2a}$$

$$E_j^R(z_j) = E_j^R(0)\exp(ik_j \sin\theta_j z_j) = E_j^R(0)\exp\left(i\frac{1}{2}Q_j z_j\right). \tag{7.2b}$$

The amplitude factors (or retardation factors),

$$a_j = \exp\left(-i\frac{1}{2}Q_j(t_j - z_j)\right) \quad \text{and} \quad b_{j+1} = \exp\left(-i\frac{1}{2}Q_{j+1} z_{j+1}\right), \tag{7.3}$$

1 account for the phase retardation effects incurred by the waves traveling to
2 and from the $j, j+1$ boundary from depths z_j and z_{j+1} within the respective
3 layers. Using the small-angle approximation, $sin\theta_j = \theta_j$, we define

$$Q_j = Q'_j - iQ''_j = \frac{4\pi}{\lambda_1} n_j \theta_j = \frac{4\pi}{\lambda_1}\sqrt{\theta_1^2 - 2(\delta_j + i\beta_j)} \tag{7.4}$$

4 as the complex scattering vector inside the jth layer. In the top vacuum (air)
5 layer; $Q_1 = 4\pi\theta_1/\lambda_1 = 4\pi\theta/\lambda = Q$. The solution to the two simultaneous
6 equations in Eq. (7.1) leads to a recursion formula

$$A_{j,j+1} = a_j^2 b_j^2 \left[\frac{A_{j+1,j+2} + F^R_{j,j+1}}{A_{j+1,j+2}F^R_{j,j+1} + 1}\right], \tag{7.5}$$

7 where

$$A_{j,j+1} = b_j^2 \frac{E_j^R(z_j)}{E_j(z_j)} = \frac{E_j^R(0)}{E_j(0)} = \frac{|E_j^R(0)|e^{i\varphi_j^R}}{|E_j(0)|e^{i\varphi_j}} = \left|\frac{E_j^R(0)}{E_j(0)}\right| e^{iv_j}. \tag{7.6}$$

8 The Fresnel coefficients for reflectivity and transmission at the $j, j+1$
9 interface are defined respectively as:

$$F^R_{j,j+1} = \frac{Q_j - Q_{j+1}}{Q_j + Q_{j+1}} \quad \text{and} \quad F^T_{j,j+1} = \frac{2Q_j}{Q_j + Q_{j+1}}. \tag{7.7}$$

10 The recursion formulation (Eq. 7.5) is solved by starting at the semi-
11 infinitely thick $j = M$ bottom layer, where $E_M^R = 0$ and hence $A_{M,M+1} = 0$.
12 At the next interface from the bottom: $A_{M-1,M} = a^2_{M-1} b^2_{M-1} F^R_{M-1,M}$. The
13 recursion is applied a total of $M - 1$ times; until we get to the top interface,
14 where

$$\frac{E_1^R(0)}{E_1(0)} = A_{1,2} \tag{7.8}$$

15 is the E-field amplitude ratio at the top interface. This is used to calculate
16 the reflectivity.

$$R = \left|\frac{E_1^R(0)}{E_1(0)}\right|^2. \tag{7.9}$$

17 Figure 7.3(a) shows the measured and calculated reflectivity for d = 21.6 nm
18 Si/Mo multilayer with $N = 15$ periods.[21,22] The topmost period of the
19 model used in this calculation is shown in Fig. 7.4.

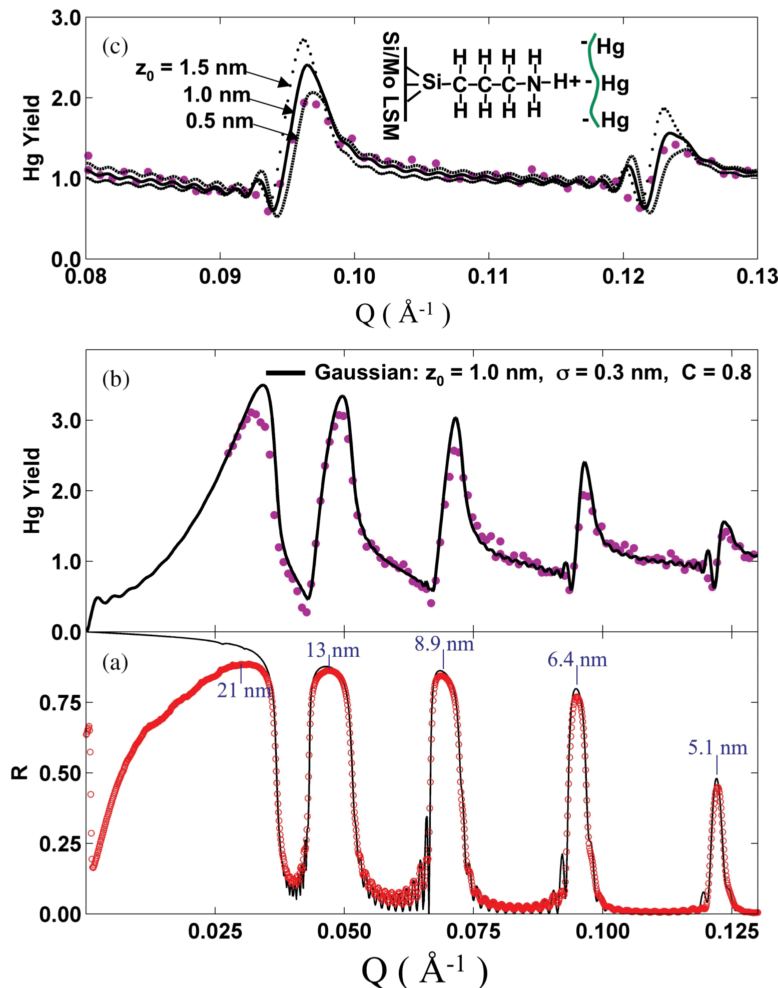

Fig. 7.3. XSW case study of Hg-labeled RNA adsorbed to an amine-terminated silica surface of a periodic multilayer. (a) Measured and calculated reflectivity for a d = 21.6 nm Si/Mo PML over a range in Q that includes the $m = 0$ to $m = 4$ Bragg peaks. The data were collected at NSLS X15A with a Ge(111) monochromator at $E_\gamma = 12.40$ keV. The continuously variable period of the XSW in the air above the PML, $D = 2\pi/Q$, is listed at each Bragg peak center. Referring to the inset in (c), the top silica surface was coated with an amine-terminated self-assembled monolayer (SAM) to which mercurated polyuridylic acid (Hg-poly(U)) was adsorbed from a 165 μM solution. After a 10-min incubation period, the surface was blown dry and the *ex situ* data shown in (a–c) was collected. The analysis of the Hg Lα yield shown in (b–c) shows that 80% of the RNA molecules lie atop the SAM with a height of 1.0 nm above the silica surface and with a Gaussian layer thickness of $\sigma = 0.3$ nm. See Ref. 21 for details.

November 15, 2011 17:20 The X-ray Standing Wave Technique: Principles and Applications 9inx6in b1281-ch07 1st Reading

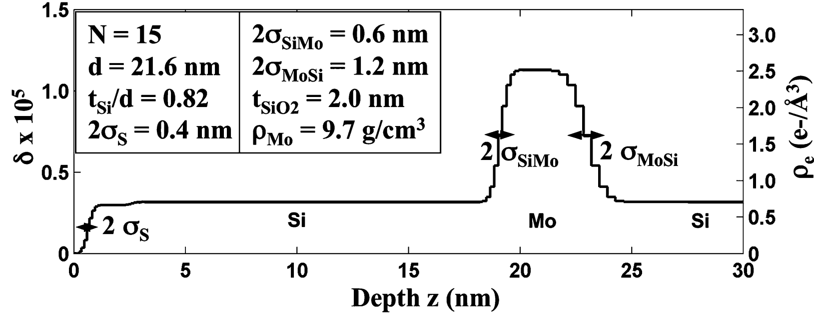

Fig. 7.4. The model used for calculating the reflectivity, E-field intensity, and XRF yield curves shown in Figs. 7.3 and 7.5. This is the electron density profile for the topmost period of the Si/Mo multilayer. The model also includes a 2-nm SiO_x layer at the air interface. From the model δ_j, β_j, and t_j are calculated for each layer in a graded interface model. The parameters listed in the inset were determined from the reflectivity fit in Fig. 7.3(a). See Refs. 21 and 22 for details.

The E-field intensity at depth z_j within the jth layer is:

$$\begin{aligned} I_j(Q, z_j) &= |E_j(z_j) + E_j^R(z_j)|^2 \\ &= |E_j(0)|^2 e^{-Q_j'' z_j} \left\{ 1 + \left| \frac{E_j^R(z_j)}{E_j(z_j)} \right|^2 + 2 \left| \frac{E_j^R(z_j)}{E_j(z_j)} \right| \cos(v_j - Q_j' z_j) \right\}. \end{aligned} \tag{7.10}$$

From Eq. (7.6), the modulus and relative phase of the E-field amplitude ratio are respectively defined as:

$$\left| \frac{E_j^R(z_j)}{E_j(z_j)} \right| = \left| \frac{E_j^R(0)}{E_j(0)} \right| e^{2Q_j'' z_j} = |A_{j,j+1}| e^{2Q_j'' z_j} \tag{7.11}$$

$$v_j = \arg(A_{j,j+1}). \tag{7.12}$$

If we normalize the incident intensity to unity, i.e., set $|E_1(0)|^2 = 1$, the intensity in the transmitted E-field at the top of the jth layer is:

$$|E_j(0)|^2 = \prod_{m=1}^{j-1} |T_{m,m+1}|^2 e^{-Q_m'' t_m}, \tag{7.13}$$

where

$$T_{j,j+1} = \frac{E_{j+1}(0)}{E_j(t_j)} = \frac{1}{F_{j,j+1}^T} \left[1 - e^{iQ_j t_j} F_{j,j+1}^R A_{j,j+1} \right]. \tag{7.14}$$

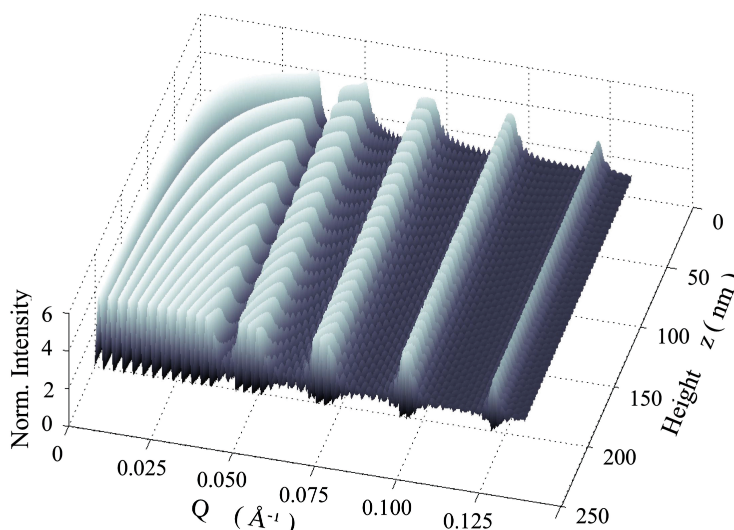

Fig. 7.5. The E-field intensity, I(Q,z), in layer $j = 1$ (air) calculated from Eq. (7.10) for the multilayer described in Fig. 7.4 with reflectivity shown in Fig. 7.3(a). Notice how the XSW period decreases at successively higher values of "Q".

Figure 7.5 shows the calculated E-field intensity for the $d = 21.6$ nm Si/Mo multilayer described in Fig. 7.4. The height coordinate z in Fig. 7.5 and z_0 in Fig. 7.3(b–c) use the same origin as used for the depth coordinate in Fig. 7.4.

7.3. Analysis of the XRF Yield

The XRF yield from a distribution of atoms, $\rho(z)$, within the multilayer is

$$Y(Q) = \int \rho(z) I(Q, z) e^{-\mu_F z/\sin\alpha} dz, \quad (7.15)$$

where μ_F and α are, respectively, the linear absorption coefficient and take-off angle for the emitted fluorescent X-rays.

The example XRF yield shown in Fig. 7.3(b) and 7.3(c) is for Hg-labeled RNA molecules adsorbed to an amine-terminated self-assembled monolayer that was grown on the top silica layer of the multilayer described in Fig. 7.4, Ref. 21. The modeled distribution, $\rho(z)$, for Hg atoms in this case study was partitioned into two parts. A fraction, C, of Hg atoms were assigned to occupy a Gaussian distribution with mean-height z_0 above the silica surface and width σ. The $(1 - C)$ remaining fraction of Hg atoms were set

to occupy a uniform distribution extending from $z = 0$ to $z = 200\,\text{nm}$. The best fit value of $z_0 = 1.0\,\text{nm}$ is in reasonable agreement with the expected thickness of the primer layer and the RNA molecular radius. The sensitivity of the measurement of this parameter at the $m = 3$ and $m = 4$ Bragg peaks is demonstrated in Fig. 7.3(c). The fact that the Hg distribution profile width was only $\sigma = 0.3\,\text{nm}$ is consistent with the electrostatic attraction between the RNA polyanions and the positively charged amine groups at the surface.

In the above case study, a simple over-layer configuration that had no measurable effect on the X-ray reflectivity was used to demonstrate the XSW technique using periodic multilayers. However, many overlayer structures do have a significant effect on the reflectivity and must therefore be included in the reflectivity modeling step.[4,5,22] In this case, the unknown overlayer structure is determined using an iterative process of reflectivity-fitting followed by determination of the element distribution using XSW. In such cases the E-field intensity, I(Q,z) is calculated inside the layer representing the unknown overlayer. This method is also able to successfully treat cases in which a resonant cavity occurs.[22,23]

Acknowledgments

Colleagues who inspired and assisted this work include G. Mark Bommarito, Donald Bilderback, Boris Batterman, Martin Caffrey, Hector Abruna, Jin Wang, Thomas Penner, Jay Schildkraut, Chian Liu, Ray Conley, Hao Cheng, Kai Zhang, Monica Olvera de la Cruz, Alfonso Mondragon, and Zhong Zhong. The data in this chapter were collected at the X15A station of the National Synchrotron Light Source (NSLS), which is supported by the US Department of Energy. The work was also partially supported by the US National Science Foundation and National Institute of Health.

References

1. T. W. Barbee and W. K. Warburton, *Mater. Lett.* **3** (1984) 17.
2. M. J. Bedzyk, D. Bilderback, J. White, H. D. Abruna and M. G. Bommarito, *J. Phys. Chem.* **90** (1986) 4926.
3. M. J. Bedzyk, D. H. Bilderback, G. M. Bommarito, M. Caffrey and J. S. Schildkraut, *Science* **241** (1988) 1788.
4. J. A. Libera, R. W. Gurney, C. Schwartz, H. Jin, T. L. Lee, S. T. Nguyen, J. T. Hupp and M. J. Bedzyk, *J. Phys. Chem. B* **109** (2005) 1441.

5. J. A. Libera, H. Cheng, M. Olvera de la Cruz and M. J. Bedzyk, *J. Phys. Chem. B* **109** (2005) 23001.
6. S. K. Ghose and B. N. Dev, *Phys. Rev. B* (2001) 6324.
7. A. Iida, T. Matsushita and T. Ishikawa, *Jpn. J. Appl. Phys.* **24** (1985) L675.
8. J. B. Kortright and A. Fischer-Colbrie, *J. Appl. Phys.* **61** (1987) 1130.
9. S. I. Zheludeva, M. V. Kovalchuk, N. N. Novikova, A. N. Sosphenov, N. E. Malysheva, N. N. Salashenko, A. D. Akhsakhalyan, Y. Y. Platonov, R. I. Cernik and S. P. Collins, *Thin Solid Films* **259** (1995) 131.
10. D. K. G. de Boer, A. J. G. Leenaers and W. W. van den Hoogenhof, *X-Ray Spectrom.* **24** (1995) 91.
11. S. K. Kim and J. B. Kortright, *Phys. Rev. Lett.* **86** (2001) 1347.
12. T. W. Barbee, *Proc. Low Energy X-Ray Diagnostics* (AIP, New York, 1981), pp. 131–145.
13. B. L. Henke, *Proc. Low Energy X-Ray Diagnostics* (AIP, New York, 1981), pp. 146–155.
14. J. H. Underwood and T. W. Barbee, *Proc. Low Energy X-Ray Diagnostics* (AIP, New York, 1981), pp. 170.
15. D. H. Bilderback, B. M. Lairson, T. W. Barbee, G. E. Ice and C. J. Sparks, *Nucl. Instrum. Meth. Phys. Res.* **208** (1983) 251.
16. E. Spiller and A. E. Rosenbluth, *Opt. Engrg.* **25** (1986) 954.
17. L. G. Parratt, *Phys. Rev.* **95** (1954) 359.
18. L. Nevot and P. Croce, *Rev. Phys. Appl.* **15** (1980) 761.
19. M. Born and E. Wolf, *Principles of Optics*, 5th edn. (Pergamon Press, Oxford, 1975).
20. G. M. Bommarito, Ph.D. Thesis, Cornell University (1992).
21. J. A. Libera, Ph.D. Thesis, Northwestern University (2005).
22. J. A. Libera, R. W. Gurney, S. T. Nguyen, J. T. Hupp, C. Liu, R. Conley and M. J. Bedzyk, *Langmuir* **20** (2004) 8022.
23. J. Wang, M. J. Bedzyk and M. Caffrey, *Science* **258** (1992) 775.